


In-plane magnetic field driven conductance modulations in topological insulator kinksGerrit Behner^{1,*,} Kristof Moors^{1,†} Yong Zhang,[‡] Michael Schleenvoigt^{1,} Alina Rupp^{1,} Erik Zimmermann^{1,} Abdur Rehman Jalil^{1,} Peter Schüffelgen, Hans Lüth, Detlev Grützmacher, and Thomas Schäpers[§]*Peter Grünberg Institut 9, Forschungszentrum Jülich, D-52425 Jülich, Germany
and JARA-Fundamentals of Future Information Technology, Jülich-Aachen Research Alliance,
Forschungszentrum Jülich and RWTH Aachen University, Germany* (Received 8 November 2023; revised 20 February 2024; accepted 5 April 2024; published 23 April 2024)

We present low-temperature magnetoconductance measurements on $\text{Bi}_{1.5}\text{Sb}_{0.5}\text{Te}_{1.8}\text{Se}_{1.2}$ kinks with ribbon-shaped legs. The conductance displays a clear dependence on the in-plane magnetic field orientation. The conductance modulation is consistent with orbital effect-driven trapping of the topological surface states on different side facets of the legs of the kink, which affects their transmission across the kink. This magnetic field driven trapping and conductance pattern can be explained with a semiclassical picture and is supported by quantum transport simulations. The interpretation is corroborated by varying the angle of the kink and analyzing the temperature dependence of the observed magnetoconductance pattern, indicating the importance of phase coherence along the cross-section perimeter of the kink legs.

DOI: [10.1103/PhysRevB.109.155429](https://doi.org/10.1103/PhysRevB.109.155429)**I. INTRODUCTION**

Three-dimensional topological insulators (3D TIs) are a class of materials in which strong spin-orbit coupling leads to a band inversion in the bulk electronic band structure [1,2]. This in turn causes the appearance of gapless surface states protected by time-reversal symmetry. Topological insulators are particularly interesting for applications in topological quantum computer architectures [3–7]. These circuits typically consist of networks of topological insulator nanoribbons combined with superconducting electrodes [8–14]. In this context, the electronic transport behavior of nanoribbons as well as more complex structures such as kinks and junctions of nanoribbons is of high interest.

In nanoribbon structures, the existence of topological surface states is revealed by magnetotransport measurements [15–22]. Here, regular Aharonov-Bohm oscillations are observed when an axial magnetic field is applied, due to the presence of closed-loop surface states. The appearance of Aharonov-Bohm oscillations also confirms that the transport in the surface states is phase coherent with a phase-coherence length of the order of a few-hundred nanometers [17,18,21,22]. For three-dimensional topological insulators, the surface transport is often accompanied by a transport channel carried by bulk carriers due to intrinsic doping effects [23,24]. In this respect, nanostructures offer a unique advantage as their surface-to-volume ratio increases and the bulk and surface conductance contributions can be disentangled

in transport experiments. In 3D TI nanoribbon-based three-terminal junctions, it has been experimentally shown that the conductance can be steered by applying an in-plane magnetic field [25]. This steering effect is attributed to the interplay between the phase-coherent transport in topological surface states and an orbital effect on the side facets of the nanoribbon. This causes electrons in the surface states to be trapped on the upper or lower surface of a nanoribbon, depending on the relative orientation of each nanoribbon leg with respect to the in-plane magnetic field.

Analogously to the effect of the in-plane field on the conductance in three-terminal junctions, the theoretical models also predict a π -periodic change in the conductance of a 3D TI nanoribbon-based kink under rotation of an in-plane magnetic field [26]. To address this issue, we have studied the low-temperature magnetotransport properties of quaternary $\text{Bi}_{1.5}\text{Sb}_{0.5}\text{Te}_{1.8}\text{Se}_{1.2}$ kinks with different angles between the input and output terminal. Quaternary materials have been shown to suppress the bulk conductivity in previous studies [27–29]. The devices were fabricated using a selective-area molecular beam epitaxy (MBE) approach. The modulation of the conductance was then measured as a function of the angle of the applied in-plane magnetic field with respect to the orientation of the device. The experimental results are interpreted on the basis of a semiclassical theoretical model and corresponding simulations [25].

II. METHODS

The $\text{Bi}_{1.5}\text{Sb}_{0.5}\text{Te}_{1.8}\text{Se}_{1.2}$ layer was grown by molecular beam epitaxy; a selective-area growth (SAE) approach was employed to yield the desired structures [20,30,31]. The samples are prepared in a three-step process. First, the substrate is prepared with a 5-nm-thick thermal SiO_2 layer and a 20-nm-thick plasma-enhanced chemical vapor deposition (PECVD)

*g.behner@fz-juelich.de

†k.moors@fz-juelich.de

‡On leave from: School of Information Science and Technology, ShanghaiTech University, Shanghai, China.

§th.schaeppers@fz-juelich.de

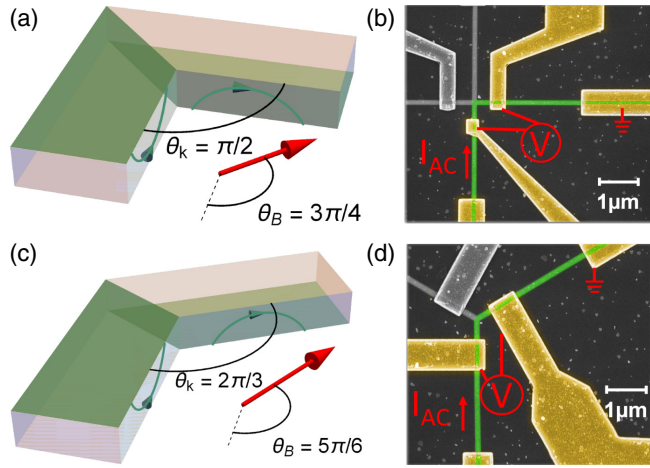


FIG. 1. (a) Schematic of the 90° kink. The red arrow indicates the orientation of the magnetic field with respect to the kink structure. The magnetic field angle θ_B is set to $\theta_B = 3\pi/4$, which is the position for minimum transmission in the kink structure. The green surfaces on the legs of the kink indicate the trapping on opposite sides (reducing the transmission) of the surface-state channels due to the orbital effect of the external magnetic field. (b) Scanning electron micrograph of the 90° kink devices. Note that the spare electrodes (in gray) were kept as open contacts in order to avoid any interference. The red annotations indicate the measurement setup. (c) Corresponding schematic of the 120° kink, with the red arrow indicating the magnetic field angle of $\theta_B = 5\pi/6$. (d) Scanning electron micrograph of the 120° kink devices.

Si_3N_4 layer to form the selective-area growth mask. The shape of the SAE trench is defined using reactive ion etching (CHF_3/O_2) and hydrofluoric acid wet etching after an electron beam lithography step. This is done in order to reveal the $\text{Si}(111)$ surface as well as to passivate it before the growth. To prevent oxidation, the film is capped using a 5-nm-thick AlO_x layer. The kink structure is contacted with 70 nm Ti contacts via *ex situ* electron beam evaporation. Structures with a kink angle of 90° and 120° are investigated, which are part of a cross and symmetric three-terminal structure, respectively. Figures 1(a) and 1(c) show the corresponding schematic illustration of the kink structures, together with the definitions of the kink θ_k and magnetic field angles θ_B , respectively. In Figs. 1(b) and 1(d), scanning electron beam micrographs of the 90° and the 120° kink structure are shown.

From Hall measurements at 1.5 K, we determined a carrier concentration of $2.3 \times 10^{13} \text{ cm}^{-2}$ and a mobility of $155 \text{ cm}^2/\text{Vs}$ (see Supplementary Note 1 of Ref. [32]). These properties are attributed to the coexistence of diffusive bulk- and quasiballistic surface states in the material [33]. Transport in the micrometer-sized Hall devices is dominated by the diffusive bulk states. The Ohmic contacts are formed by a 70-nm-thick Ti layer. Before deposition of the metal layer, the AlO_x capping in the contact areas was removed by wet chemical etching and argon sputtering.

The measurements were carried out in a variable temperature insert with a base temperature of 1.5 K. The conductance of the device was measured using a standard four-probe lock-in setup [cf. Figs. 1(b) and 1(d)]. The rotation of the in-plane

magnetic field with respect to the kink structure was realized by employing a mechanically rotatable sample rod, where the sample was rotated by π in 19 steps. After each step, the magnetic field was swept from -12 T to 12 T in order to realize an effective rotation of the magnetic field of 2π .

The simulations of the conductance in the kink structures are based on a semiclassical theoretical model that is explained in detail in Ref. [25]. We consider a subband-quantized Dirac surface-state spectrum that is appropriate for the cross-section geometry of the 3D TI kink legs and a Dirac point that is separated from the Fermi level by 0.1 eV.

III. MAGNETOCONDUCTANCE

Figure 2(a) shows the measured conductance in units of G_0 of the 90° kink as a function of magnetic field, with $G_0 = 2e^2/h$, where e is the electron charge and h is Planck's constant. The measurements were taken at a temperature of 1.5 K. Each color-coded line represents a single measurement between -12 T and 12 T for a different in-plane magnetic field angle ranging from 0 to π . The definition of the in-plane magnetic field angle θ_B with respect to the sample is given in Fig. 1(a).

All of the magnetoconductance traces shown in Fig. 2(a) exhibit several prominent features. The conductance peak at zero magnetic field can be attributed to the weak antilocalization effect [34]. This peak structure has previously been observed in topological insulator nanoribbon structures [20]. It is due to electron interference after scattering on impurities in combination with the strong spin-orbit coupling of the material. The small fluctuations of the conductance over larger magnetic field intervals represent universal conductance fluctuations [35]. These are caused by the interference of a finite number of trajectories due to the small dimensions of the sample. Apart from these two features observed in each curve, the color-coded magnetic field sweeps also reveal a change in resistance with a change in the magnetic field angle θ_B . In order to analyze the dependence of the magnetoconductance on the magnetic field orientation in detail, the data are plotted in the style of a color map as a function of the absolute magnetic field $|B|$ and the magnetic field angle θ_B . Here, we consider only the effective conductance change $\Delta G/G_0$ defined by

$$\Delta G/G_0 = [G(B, \theta_B) - \langle G(B, \theta_B) \rangle_{\theta_B}] / G_0, \quad (1)$$

which is the normalized difference between the conductance at a certain magnetic field and in-plane field angle, $G(B, \theta_B)$, and the average conductance at constant magnetic field averaged over all angles, $\langle G(B, \theta_B) \rangle_{\theta_B}$. Figure 2(b) shows the effective conductance for the 90° kink. A clear π -periodic variation of the conductance with a variation of the in-plane magnetic field angle is visible. The areas of maximum and minimum conductance are centered around the values of $-\pi/4$, $3\pi/4$ and $\pi/4$, $-3\pi/4$, respectively. The $\theta_B = 3\pi/4$ field orientation for the minimum conductance case is indicated in Fig. 1(a). In order to demonstrate that the change in magnetoconductance is not a result of an angular dependence of universal conductance fluctuations (UCFs), a detailed analysis of the root-mean-square value of the conductance fluctuations, δ_{GRMS} , is provided in the Supplemental

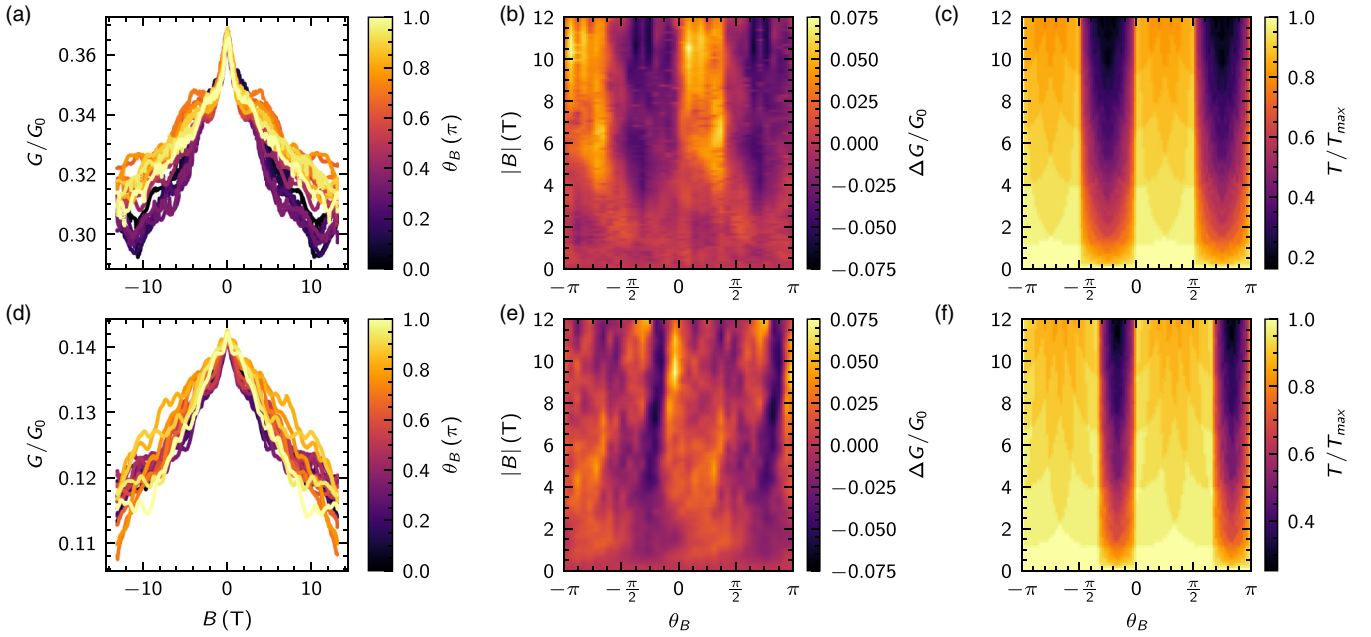


FIG. 2. Conductance of the 90° and 120° kink structures at 1.5 K. (a) Conductance of the 90° kink in units of $G_0 = 2e^2/h$ as a function of the in-plane magnetic field. The single lines are color coded, where the color represents the angle under which the magnetic field is applied with respect to the device. (b) Color map of the effective conductance $\Delta G/G_0$ [see Eq. (1)] of the 90° kink as a function of magnetic field angle θ_B and absolute magnetic field $|B|$. (c) Calculated normalized transmission T/T_{\max} as a function of absolute magnetic field $|B|$ and magnetic field angle θ_B . (d)–(f) Corresponding plots for the 120° kink.

Material [36]. We refer the reader to Ref. [25] for an analysis of the angle dependence of UCFs in a similar material system.

In the following, a kink with a larger angle between the input and output terminals, i.e., a 120° kink, is analyzed. The corresponding normalized magnetoconductance as a function of magnetic field for in-plane angles between 0 and π is shown in Fig. 2(d). Similar to the conductance of the 90° kink, a clear modulation of the conductance with the variation of the in-plane field angle can be seen. Analogous to the first device, these data are converted to the effective conductance change using Eq. (1). Figure 2(e) shows the effective magnetoconductance of the 120° kink. A shift of the position of the minimum and maximum conductance compared to measurements shown in Fig. 2(b) for the 90° kink is observed. The experimentally observed modulations match well with the theoretically expected positions for maximum and minimum conductance, i.e., $-\pi/6, 5\pi/6$ and $-2\pi/3, \pi/3$, respectively. The positions are derived from trivial geometrical considerations regarding the aligned and transverse orientation of the magnetic field with respect to the kink angle.

To explain the origin of the angle-modulated conductance pattern, we consider the impact of the orbital effect on the topological surface states in a semiclassical picture [25], analogous to the treatment of the steering effect in a topological insulator-based T junction in Ref. [26]. On the top and bottom facets of the ribbon, the Lorentz force points perpendicular to the surface and can be neglected for surface-state motion that is bound to the surface of the ribbon. On the side facets (assumed to be perpendicular to the plane here), however, the Lorentz force induces a circular motion of the charge carriers [see Figs. 1(a) and 1(c)]. Depending on the transverse velocity of the surface state, the carriers will or will not be able to

traverse the side facet from bottom to top (or vice versa). Thus, when the transverse extent is smaller than the height of the ribbon, the carriers cannot traverse the side facet. For surface states that wrap phase-coherently around the perimeter of the ribbon cross section, it follows that the top or bottom surface effectively gets depleted or, equivalently, carriers are trapped on the opposite surface. When the carriers on the two legs of the kink are trapped on opposite facets of the ribbon, the transmission across the kink is suppressed, as illustrated in Figs. 1(a) and 1(c). This is also demonstrated by quantum transport simulations in the Supplemental Material of Ref. [25]. In Figs. 2(c) and 2(f), the calculated normalized transmission T/T_{\max} as a function of magnetic field angle θ_B and absolute magnetic field $|B|$ is given for the 90° kink and 120° kink structures, respectively (see Supplemental Material [36] for details). By comparing Figs. 2(b) and 2(e), one finds that the experimental results nicely follow the transmission pattern that results from the semiclassical picture. Comparing the simulations as well as the effective conductance color maps in Figs. 2(b) and 2(e), it is clear that the range of angles with reduced conductance becomes narrower for an increased kink angle. This is consistent with the picture based on the Lorentz force inducing a trapping effect via the side facets. The window of angles for which the Lorentz force has opposite sign on the side facets of the two legs of the kink (yielding an opposite trapping effect in each leg and a reduced transmission probability across the kink) naturally narrows down when the legs become more aligned. The relevant angle window corresponds to $\theta_B \in [\pi/2, \pi] + n\pi$ for the 90° kink, and to $\theta_B \in [3\pi/2, \pi] + n\pi$ for the 120° kink.

Compared to our previous study [25], the high magnetic field ranges of the experiment allow for the sample to get into

a regime where the gyroradius is of the order of the ribbon height (approximately 20 nm). This drastically increases the effective conductance change between the default and suppressed transport regimes to about 8% (increased by more than an order of magnitude).

In the Supplemental Material of Ref. [25], it was also shown that the steering effect is only expected for states that are located on the surface, and that the robustness of the effect against disorder is highly enhanced by spin-momentum locking, which suppresses scattering processes with a significant change in momentum. The observed magnetoconductance pattern is therefore not likely to originate from trivial bulk states or trivial surface states without spin-momentum locking. Hence, in-plane magnetic field dependence of the conductance across the kink structures provides a robust transport signature of topological surface states.

For a more detailed comparison of the angle-dependent conductance pattern between the experimental results and the simulations, we take linecuts at certain magnetic fields. Figure 3 displays linecuts of the effective conductance change $\Delta G/G_0$ in comparison to linecuts of the normalized transmission at magnetic fields ranging from 2 to 10 T, respectively, as a function of in-plane magnetic field angle. Note that the normalized transmission is rescaled and shifted to fit the scale of the conductance changes in order to compare the angle-dependent π -periodic pattern. At the linecuts above 2 T, simulation and experiment are in very good agreement. For magnetic field strengths of 2 T and less, no periodic behavior of the effective conductance can be seen [cf. Fig. 2(c)].

Figure 4 shows the temperature-dependent effective conductance of the 90° kink for four different temperatures, ranging from 1 to 20 K. The color scheme for all temperatures is normalized to that of the 1 K measurement. From previous work performed on similar devices, it was found that charge carriers are located phase-coherently around the perimeter of a ribbon of similar height up to temperatures of about 20 K [37]. Therefore, the temperature range allows us to probe the proposed effect in the transition of the phase-coherent regime to a regime where an increased amount of inelastic scattering events occur. The temperature dependence of the effect matches the expected behavior for an effect that relies on phase coherence around the perimeter of the ribbon. A vanishing periodic conductance change is visible, with the pattern completely disappearing at temperatures above 20 K. The impact of the in-plane magnetic field on the conductance due to trapping of the surface states on certain side facets of the nanoribbon is only expected to occur when the surface states are phase coherent around the perimeter of the ribbon, i.e., at sufficiently low temperatures. At elevated temperatures, the phase-coherence length reduces so that the surface states on the different side facets are effectively becoming independent and there can be no depletion of surface states on either top or bottom surface of the ribbon through a Lorentz force acting on the side facets.

To emphasize that the trapping effect can be associated with the phase coherence of the surface states, we plot the average conductance G_{av} (over all magnetic field strengths and angles) of the device as a function of temperature and compare it with the peak-to-valley difference of conductance over different in-plane magnetic field angles [see Fig. 4(e)].

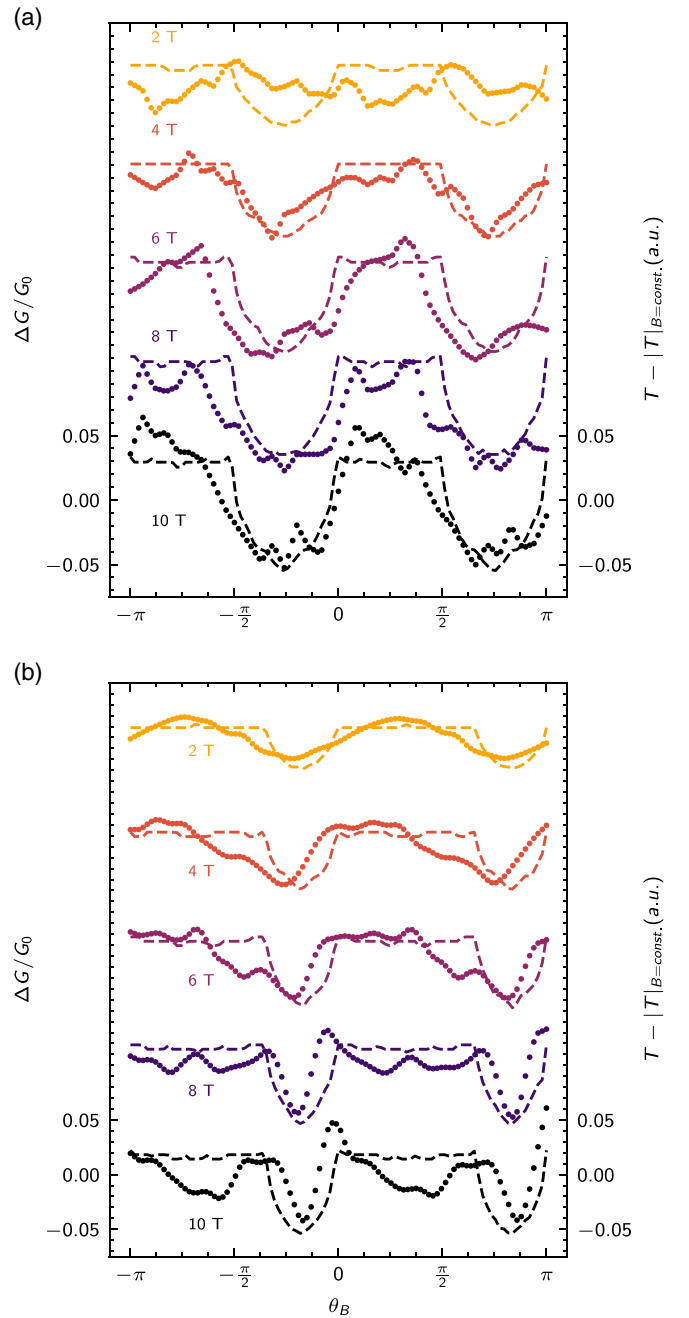


FIG. 3. Linecuts of the effective conductance change $\Delta G/G_0$ (dotted lines) and of the normalized transmission $T - |T|_{B=const}$ (dashed lines) as a function of θ_B at magnetic fields ranging from 2 to 10 T in steps of 2 T for the (a) 90° and (b) 120° kink (taken from Fig. 2). Note that the individual curves are offset for better clarity.

The peak-to-valley difference ΔG_{θ_B} is obtained by taking the difference between the conductance averaged over $\theta_B \in [0, \pi/2] + n\pi$ (peak) and over $\theta_B \in [\pi/2, \pi] + n\pi$ (valley) for all magnetic field strengths $B > 4$ T. While the average conductance of the sample is barely affected by temperature (and phase coherence around the perimeter), the peak-to-valley difference decreases exponentially with temperature towards zero. This is similar to the temperature dependence of Aharonov-Bohm oscillations, for example, $\propto \exp[-P/l_\phi(T)]$, with perimeter P and temperature-dependent phase-coherence

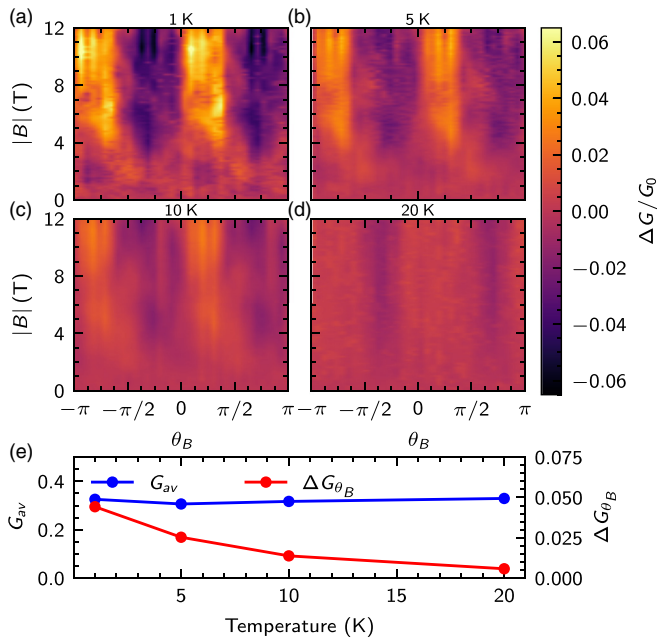


FIG. 4. (a)–(d) Effective normalized conductance $\Delta G/G_0$ of the 90° kink as a function of θ_B and B at (a) 1, (b) 5, (c) 10, and (d) 20 K. The periodic pattern as a function of in-plane magnetic field angle is clearly vanishing with increasing temperature. (e) The peak-to-valley difference ΔG_{θ_B} averaged over all magnetic fields in comparison to the average conductance G_{av} of the sample averaged over all angles and magnetic fields. These values are displayed as a function of temperature. It is clearly visible that the average conductance of the sample is rather constant with increasing temperature, whereas the peak-to-valley difference exponentially drops to zero.

length $l_\phi(T)$, which also naturally depend on the phase coherence around the perimeter [33].

Note that an out-of-plane component of the magnetic field, due to a small misalignment between the plane of rotation of the magnetic field and the plane of the kink structure, for example, is unlikely to be responsible for the observed conductance pattern for the following reasons. First, our setup ensures good alignment between the kink structure and the external magnetic field (a misalignment of, at most, 2 degrees). Second, such misalignment would yield a sinusoidal dependence on θ_B for the out-of-plane component, with no qualitative difference for different kink angles (unlike the measured patterns). Furthermore, the observed minima and maxima of the conductance would only match the expected angles (based on the trapping effect) coincidentally. Third,

a conventional magnetoresistance related to an out-of-plane magnetic field component would not have a strong temperature dependence that indicates a connection with phase coherence of the surface states around the perimeter of the legs of the kink.

IV. CONCLUSION

In conclusion, for 3D topological nanoribbon-based 90° and 120° kink structures, we observed pronounced modulations in the conductance upon varying the in-plane magnetic field orientation. From the decrease of the modulation pattern with increasing temperature, we deduced that the effect is based on phase-coherent carriers. In a semiclassical picture, the modulations can be explained by an orbital effect trapping electrons in the topological surface states either on the upper or lower surface of the nanoribbon legs, which affects their transmission probability across the kink. Our experimental results are in good agreement with the theoretically expected transport behavior and consistent with the differences expected for different kink angles. The transport properties of TI nanoribbon-based kinks with an in-plane magnetic field offer interesting perspectives for the design of topological quantum circuits. The orbital effect could be exploited to drive a kink-shaped TI Josephson junction into the topological regime with Majorana states, while also offering a tuning knob for the Josephson energy through modulation of the surface-state transparency.

ACKNOWLEDGMENTS

We thank Herbert Kertz for technical assistance, and Florian Lentz and Stefan Trelenkamp for electron beam lithography. This work was partly funded by the Deutsche Forschungsgemeinschaft (DFG, German Research Foundation) under Germany’s Excellence Strategy - Cluster of Excellence Matter and Light for Quantum Computing (ML4Q) EXC 2004/1 – Grant No. 390534769. K.M. acknowledges the financial support by the Bavarian Ministry of Economic Affairs, Regional Development and Energy within Bavaria’s High-Tech Agenda Project “Bausteine für das Quantencomputing auf Basis topologischer Materialien mit experimentellen und theoretischen Ansätzen” (Grant No. 07 02/686 58/1/21 1/22 2/23). P.S. and K.M. acknowledge financial support by the German Federal Ministry of Education and Research (BMBF) via the Quantum Futur project “MajoranaChips” (Grant No. 13N15264) within the funding program Photonic Research Germany.

[1] M. Z. Hasan and C. L. Kane, *Rev. Mod. Phys.* **82**, 3045 (2010).
 [2] X.-L. Qi and S.-C. Zhang, *Rev. Mod. Phys.* **83**, 1057 (2011).
 [3] C. Nayak, S. H. Simon, A. Stern, M. Freedman, and S. Das Sarma, *Rev. Mod. Phys.* **80**, 1083 (2008).
 [4] J. Alicea, *Rep. Prog. Phys.* **75**, 076501 (2012).
 [5] T. Hyart, B. van Heck, I. C. Fulga, M. Burrello, A. R. Akhmerov, and C. W. J. Beenakker, *Phys. Rev. B* **88**, 035121 (2013).

[6] S. D. Sarma, M. Freedman, and C. Nayak, *npj Quantum Inf.* **1**, 15001 (2015).
 [7] D. Aasen, M. Hell, R. V. Mishmash, A. Higginbotham, J. Danon, M. Leijnse, T. S. Jespersen, J. A. Folk, C. M. Marcus, K. Flensberg, and J. Alicea, *Phys. Rev. X* **6**, 031016 (2016).
 [8] A. Cook and M. Franz, *Phys. Rev. B* **84**, 201105(R) (2011).
 [9] A. M. Cook, M. M. Vazifeh, and M. Franz, *Phys. Rev. B* **86**, 155431 (2012).

- [10] J. Manousakis, A. Altland, D. Bagrets, R. Egger, and Y. Ando, *Phys. Rev. B* **95**, 165424 (2017).
- [11] F. de Juan, J. H. Bardarson, and R. Ilan, *SciPost Phys.* **6**, 060 (2019).
- [12] H. F. Legg, D. Loss, and J. Klinovaja, *Phys. Rev. B* **104**, 165405 (2021).
- [13] H. F. Legg, D. Loss, and J. Klinovaja, *Phys. Rev. B* **105**, 155413 (2022).
- [14] D. Heffels, D. Burke, M. R. Connolly, P. Schüffelgen, D. Grützmacher, and K. Moors, *Nanomaterials* **13**, 723 (2023).
- [15] H. Peng, K. Lai, D. Kong, S. Meister, Y. Chen, X.-L. Qi, S.-C. Zhang, Z.-X. Shen, and Y. Cui, *Nat. Mater.* **9**, 225 (2010).
- [16] F. Xiu, L. H. Wang, L. Cheng, L.-T. Chang, M. Lang, G. Huang, X. Kou, Y. Zhou, X. Jiang, Z. Chen, J. Zou, A. Shailos, and K. L. Wang, *Nat. Nanotechnol.* **6**, 216 (2011).
- [17] J. Dufouleur, L. Veyrat, A. Teichgräber, S. Neuhaus, C. Nowka, S. Hampel, J. Cayssol, J. Schumann, B. Eichler, O. G. Schmidt, B. Büchner, and R. Giraud, *Phys. Rev. Lett.* **110**, 186806 (2013).
- [18] Y. C. Arango, L. Huang, C. Chen, J. Avila, M. C. Asensio, D. Grützmacher, H. Lüth, J. G. Lu, and T. Schäpers, *Sci. Rep.* **6**, 29493 (2016).
- [19] L. A. Jauregui, M. T. Pettes, L. P. Rokhinson, L. Shi, and Y. P. Chen, *Sci. Rep.* **5**, 8452 (2015).
- [20] J. Kölzer, D. Rosenbach, C. Weyrich, T. W. Schmitt, M. Schleenvoigt, A. R. Jalil, P. Schüffelgen, G. Mussler, V. E. Sacksteder IV, D. Grützmacher, H. Lüth, and T. Schäpers, *Nanotechnology* **31**, 325001 (2020).
- [21] D. Rosenbach, N. Oellers, A. R. Jalil, M. Mikulics, J. Kölzer, E. Zimmermann, G. Mussler, S. Bunte, D. Grützmacher, H. Lüth, and T. Schäpers, *Adv. Electron. Mater.* **6**, 2000205 (2020).
- [22] H.-S. Kim, T.-H. Hwang, N.-H. Kim, Y. Hou, D. Yu, H.-S. Sim, and Y.-J. Doh, *ACS Nano* **14**, 14118 (2020).
- [23] D. O. Scanlon, P. D. C. King, R. P. Singh, A. de la Torre, S. M. Walker, G. Balakrishnan, F. Baumberger, and C. R. A. Catlow, *Adv. Mater.* **24**, 2154 (2012).
- [24] P. Lošťák, Z. Starý, J. Horák, and J. Pancfř, *Phys. Stat. Sol. (a)* **115**, 87 (1989).
- [25] J. Kölzer, K. Moors, A. R. Jalil, E. Zimmermann, D. Rosenbach, L. Kibkalo, P. Schüffelgen, G. Mussler, D. Grützmacher, T. L. Schmidt, H. Lüth, and T. Schäpers, *Commun. Mater.* **2**, 1 (2021).
- [26] K. Moors, P. Schüffelgen, D. Rosenbach, T. Schmitt, T. Schäpers, and T. L. Schmidt, *Phys. Rev. B* **97**, 245429 (2018).
- [27] Y. S. Kim, M. Brahlek, N. Bansal, E. Edrey, G. A. Kapilevich, K. Iida, M. Tanimura, Y. Horibe, S.-W. Cheong, and S. Oh, *Phys. Rev. B* **84**, 073109 (2011).
- [28] Z. Ren, A. A. Taskin, S. Sasaki, K. Segawa, and Y. Ando, *Phys. Rev. B* **84**, 165311 (2011).
- [29] T. Arakane, T. Sato, S. Souma, K. Kosaka, K. Nakayama, M. Komatsu, T. Takahashi, Z. Ren, K. Segawa, and Y. Ando, *Nat. Commun.* **3**, 636 (2012).
- [30] J. Kampmeier, C. Weyrich, M. Lanius, M. Schall, E. Neumann, G. Mussler, T. Schäpers, and D. Grützmacher, *J. Cryst. Growth* **443**, 38 (2016).
- [31] A. R. Jalil, P. Schüffelgen, H. Valencia, M. Schleenvoigt, C. Ringkamp, G. Mussler, M. Luysberg, J. Mayer, and D. Grützmacher, *Nanomaterials* **13**, 354 (2023).
- [32] E. Zimmermann, J. Kölzer, M. Schleenvoigt, D. Rosenbach, G. Mussler, P. Schüffelgen, T. Heider, L. Plucinski, J. Schubert, H. Lüth, D. Grützmacher, and T. Schäpers, *Semicond. Sci. Technol.* **38**, 035010 (2023).
- [33] G. Behner, A. R. Jalil, D. Heffels, J. Kölzer, K. Moors, J. Mertens, E. Zimmermann, G. Mussler, P. Schüffelgen, H. Lüth, D. Grützmacher, and T. Schäpers, *Nano Lett.* **23**, 6347 (2023).
- [34] S. Hikami, A. I. Larkin, and Y. Nagaoka, *Prog. Theor. Phys.* **63**, 707 (1980).
- [35] P. A. Lee, A. D. Stone, and H. Fukuyama, *Phys. Rev. B* **35**, 1039 (1987).
- [36] See Supplemental Material at <http://link.aps.org/supplemental/10.1103/PhysRevB.109.155429> for a detailed discussion of the effective trapping model and the choice of Fermi level used in the modeling. A comparison between conductance oscillations due to UCF and trapping effect is also provided.
- [37] D. Rosenbach, K. Moors, A. R. Jalil, J. Kölzer, E. Zimmermann, J. Schubert, S. Karimzadah, G. Mussler, P. Schüffelgen, D. Grützmacher, H. Lüth, and T. Schäpers, *SciPost Phys. Core* **5**, 017 (2022).